



UNIVERSITY OF LEEDS

This is a repository copy of *Crustal architecture of the Laptev Rift System in the East Siberian Arctic based on 2D long-offset seismic profiles and gravity modelling*.

White Rose Research Online URL for this paper:
<http://eprints.whiterose.ac.uk/120750/>

Version: Accepted Version

Article:

Drachev, SS, Mazur, S, Campbell, S et al. (3 more authors) (2018) Crustal architecture of the Laptev Rift System in the East Siberian Arctic based on 2D long-offset seismic profiles and gravity modelling. *Petroleum Geoscience*, 24 (4). pp. 402-413. ISSN 1354-0793

<https://doi.org/10.1144/petgeo2016-143>

© 2018 The Author(s). Published by The Geological Society of London for GSL and EAGE. All rights reserved. This is an author produced version of a paper published in *Petroleum Geoscience*. Uploaded in accordance with the publisher's self-archiving policy.

Reuse

Items deposited in White Rose Research Online are protected by copyright, with all rights reserved unless indicated otherwise. They may be downloaded and/or printed for private study, or other acts as permitted by national copyright laws. The publisher or other rights holders may allow further reproduction and re-use of the full text version. This is indicated by the licence information on the White Rose Research Online record for the item.

Takedown

If you consider content in White Rose Research Online to be in breach of UK law, please notify us by emailing eprints@whiterose.ac.uk including the URL of the record and the reason for the withdrawal request.



eprints@whiterose.ac.uk
<https://eprints.whiterose.ac.uk/>

27 The Laptev Sea is located between the Taimyr Peninsula and the New Siberian Islands in the
28 Siberian Arctic. It represents a unique tectonic setting where an active spreading ridge, the
29 Gakkel Ridge in the Eurasian oceanic basin, adjoins a continental margin (Fig. 1). The entire
30 shelf is dominated by extensional structures forming a 400 to 900-km-wide and 700 to 1,100-
31 km-long rift system, which was first inferred by Grachev (1982) soon after the spreading
32 nature of the Gakkel Ridge had been revealed (Karasik 1968, 1974). The first multi-channel
33 seismic reflection (MCS) data were acquired by the Marine Arctic Geological Expedition
34 (MAGE, Murmansk, RF) and by the Laboratory of Regional Geodynamics (LARGE,
35 Moscow, RF) in the second half of the 1980s. These data proved the existence of the rift
36 system and allowed for the delineation of several large rifts (Ivanova et al. 1990; Drachev &
37 Savostin 1994; Drachev et al. 1998). More regional MCS data were acquired by BGR
38 (Hannover, Germany) in cooperation with SevMorNefteGeophysika (SMNG, Murmansk,
39 Russia) in 1993, 1994 and 1997, allowing for better imaging of the extensional structural
40 assemblage down to a depth of 12 km and in some places, as deep as the Moho (Franke et al.
41 2000, 2001).

42 The seismic data coverage in the Laptev Sea has been significantly improved in the past
43 decade. Most of the seismic acquisition was performed by MAGE (Shkarubo & Zavarzina
44 2011; Shkarubo et al. 2014; Zavarzina et al. 2014), TGS in cooperation with DMNG (2010 to
45 2012), and ION (2010 to 2013). Some of the regional MCS profiles were acquired with long,
46 8 to 10 km seismic streamers and powerful sources, which resulted in much clearer seismic
47 imaging down to the Moho discontinuity, thereby allowing for previously unseen details of
48 the rift architecture and sedimentary infill to be revealed. However, the high number of
49 extensional faults bordering various half-grabens, grabens and complex extensional basins,
50 combined with the presence of sub-marine permafrost (Kholodov et al. 2001), has a profound
51 negative impact on the quality of the MCS data, which is very difficult to mitigate by seismic

52 data processing. The major consequence of these data quality issues is limited seismic
53 resolution in some **parts of the Ust' Lena Rift** in places where top pre-rift basement is situated
54 deeper than c. 10 km.

55 The existing geological interpretations of the MCS data suggest that thinned but continuous
56 continental crust underlies the entire Laptev Rift System (LRS), which makes it difficult to
57 explain the significant additional thickness of the syn-rift sedimentary fill present in **the Ust'**
58 **Lena Rift**. Based on well-known analogues, a rift infill thickness in a range of 13 to 15 km
59 requires hyperextension of the crust up to a point of its complete rupture and mantle
60 exhumation below some deepest parts of the rift (e.g. Brun & Beslier 1996; Whitmarsh et al.
61 2001; Péron-Pinvidic & Manatschal 2010).

62 The first attempt to constrain the amount of crustal stretching across the LRS with the use of
63 2D gravity modelling and 3D gravity inversion was published by Mazur et al. (2015). They
64 showed that the amount of crustal extension in the central and northern parts **of the Ust' Lena**
65 **Rift Basin** reached 430 and 500 km, respectively, and resulted in both the complete
66 elimination of the continental crust and mantle exhumation beneath this hyperextended basin.

67 In a recent publication, Drachev and Shkarubo (2017) attempted to illustrate the internal
68 structure of **the hyperextended Ust' Lena Rift Basin using long**-offset MCS profiles by
69 MAGE and TGS. Their model also suggests the presence of exhumed mantle in the axial
70 zone of the rift.

71 In this paper, we attempt to verify the postulated mantle exhumation by comparing a synthetic
72 gravity response from geological models built along three selected seismic profiles to the
73 observed regional gravity data compiled by Getech (Mazur et al. 2015). For this purpose, we
74 have used the two interpreted two way travel time (TWT) seismic profiles published recently

75 by Drachev and Shkarubo (2017), the MAGE A4 and TGS ARS10F04 Profiles, as well as
76 one depth-converted Profile BGR 9701 published by Franke et al. (2001).

77 Structure and Stratigraphy of the Laptev Rift System

78 The LRS consists of several wide rift basins and individual narrower rifts, which are
79 separated from each other by high-standing blocks of underlying basement. The geology of
80 this complex rift system has been considered in detail by Ivanova et al. (1990), Drachev et al.
81 (1998), Franke et al. (2000, 2001), Sekretov (2000), Drachev (2011, 2016), Shkarubo and
82 Zavarzina (2011) and Shkarubo et al. (2014). The Getech gravity anomaly map provides the
83 basis for our regional mapping of the main structural elements of the LRS (Fig. 1); from west
84 to east, the main structural elements are as follows: the Ust' Lena Rift, East Laptev Horst and
85 **Graben Province, Anisin Rift, Kotel'nyi High and New Siberian Rift.** The total width of the
86 LRS varies from 450 to 500 km **between Kotel'nyi Island and** the Lena River Delta to c. 870
87 km in its northern part (measured in a direction parallel to the steep shelf break of the
88 Amundsen Basin to Anabar Bay).

89 Ust' Lena Rift Basin

90 The Ust' Lena Rift Basin (ULRB) is the largest and the most prominent element of the LRS.
91 Its width varies from 550 km along a SW to NE-trending profile connecting the southern
92 termination of the Gakkel Ridge to Anabar Bay to c. 100 km in the Buor-Khaya Bay (Fig. 1).
93 A large region of extended crust is present between the eastern Taimyr coast and the
94 continental margin of the Nansen Basin, which we also tentatively include into the ULRB.
95 Therefore, the total length of the rift when measured in a NW to SE direction varies from c.
96 800 to c. 1150 km.

97 As illustrated by the seismic profiles and the gravity field (Figs. 1 and 2), the deepest axial
98 zone of the rift coincides with prominent gravity low A. Its width varies from 27 to 30 km,

99 and sediment thickness reaches 14 to 15 km. This zone is inferred to be underlain by either
100 exhumed serpentinized mantle or exhumed and radically thinned lower crust (Drachev &
101 Shkarubo 2017).

102 The axial zone is surrounded by structural domains dominated by tilted seismic horizons,
103 which we interpret as being a result of the brittle upper crust extensional faulting. To the east,
104 there is a 125 (MAGE profile) to 131 km (TGS profile) wide region of tilted seismic horizons
105 that is probably underlain by the main extensional detachment fault. It constitutes the eastern
106 rifted margin of the basin, which is manifested in the gravity field by positive anomaly B
107 (Fig. 1). The thickness of sediments along this marginal zone of the ULRB varies from 5 to
108 12 km (Fig. 2).

109 To the west of the axial zone, the crustal blocks and bounding faults are tilted in the opposite
110 direction, which allows us to consider this domain, gravity feature C, as the western flank of
111 the ULRB. This zone is best imaged by the TGS ARS10f04 Profile, which crosses it for c.
112 125 km. Nevertheless, this profile does not go across the entire western flank of the rift basin
113 as there is c. 70 km of the rifted domain between its western end and the first large -offset
114 normal fault just off the Taimyr coast, which is clearly seen in the gravity field (Fig. 1).
115 Therefore, the total width of the ULRB western flank is c. 195 km if measured along the
116 projected strike of the TGS profile, and c. 195 km if measured along the projected strike of
117 the MAGE A4 Profile. Positive gravity anomaly C corresponds to a zone of highly attenuated
118 lower crust, as interpreted by Drachev and Shkarubo (2017). The total sediment thickness
119 along the studied part of the western flank varies from c. 3 km or less on the top of horsts to c.
120 10 km at the transition to the axial rift zone.

121 The main detachment fault crossed by the TGS and MAGE profiles coincides with the M/V
122 Lazarev Fault previously mapped in this part of the Laptev Shelf by Franke et al. (2000,

123 2001). It is a large-offset listric fault with a pronounced convex geometry towards the east
124 and an apparent vertical throw of c. 4 to 6 km at the top basement horizon. Its geometry at
125 mid-crust level is poorly constrained due to the insufficient quality of the seismic data.
126 However, based on the observed reflectivity pattern in the lower crustal section, we assume
127 that this detachment flattens out at the middle crust level, before it bends down and penetrates
128 the lower crust, reaching the mantle. In a c. 17-km-wide zone immediately west of the
129 detachment, the syn-rift sediments rest upon the fault plane where their thickness reaches 7 to
130 8 km.

131 A 75-km-wide central zone of the ULRB along the TGS ARS10F04 Profile lacks apparent
132 seismic expression of brittle deformation, such as tilted basement blocks, and shows a very
133 thick sedimentary infill that extends down to a depth of c. 14 km (Fig. 2). Seismic reflection
134 geometries within this zone reveal a significant number of rather steep low-amplitude normal
135 faults, which affect the upper and middle parts of the section. Combined offsets along these
136 faults could apparently not accommodate the large amount of crustal thinning required to
137 provide accommodation space for as much as 15 km of sediments. Therefore, we infer that
138 the central zone of the ULRB represents a hyperextended rift basin underlain by a principal
139 exhumation detachment fault, with the fault marking the interface between the sediments and
140 the underlying ductile lower crust and/or serpentized mantle.

141 The steep low-amplitude normal faults occurring within the ULRB (Fig. 2) are considered to
142 be a younger generation of faults in comparison to the high-amplitude listric faults bounding
143 tilted blocks of basement in the lower section of the rift. The latter were formed during the
144 main stretching phase, whereas the former are probably the result of the recent extension
145 phase as many of them penetrate up-section to the sea bed.

146 East Laptev Horst and Graben Province

147 The East Laptev Horst and Graben Province (ELHGP) extends across the eastern part of the
148 Laptev Shelf and the adjoining Yana-Indigirka Lowland for c. 800 km in a north to south
149 direction, while its width increases from c. 100 km in its central part to c. 350 km in the
150 southern, onshore part. It is clearly expressed in the gravity field as a series of positive
151 anomalies corresponding to several high-standing blocks, or horsts, of the pre-rift basement
152 (the North Laptev, Stolbovoi and Shiroston Blocks), which are separated by much smaller
153 negative anomalies, revealing a series of small intervening half-grabens (Fig. 1). The TGS
154 and MAGE seismic profiles cross the large triangle-shaped North Laptev basement high,
155 which stretches from the shelf break towards Stolbovoi Island for c. 340 km and is c. 230 km
156 wide in its northern part and just c. 30 km wide in its southern part. In the gravity field, it
157 fully corresponds to anomaly D (Fig. 1).

158 In general terms, the ELHGP can be portrayed as a relatively stable region affected by
159 moderate extensional deformation. Its structure is formed by a succession of 10 to 15 km-
160 wide half-grabens and intervening horsts bounded by predominantly westward-dipping listric
161 normal faults. The majority of these faults were clearly active during the initial rift stage and
162 then were reactivated during the second, most recent extension phase, while some other faults
163 reveal the initial extension stage only. The magnitude of the fault offsets is in the range of a
164 few hundred meters, up to 2 km, while sediment thickness over the ELHGP varies from 0 m
165 over the elevated Stolbovoi Island to 3 km in several of the half-grabens located along the
166 western margin of the ELHGP.

167 Anzhu Rift Zone

168 The Anzhu Rift Zone forms a c. 650-km-long chain of interconnected large half-grabens,
169 **two-sided grabens and intervening horsts between the ELHGP and the Kotel'nyi High** – the
170 largest single high-standing block of the pre-rift basement present in this part of the shelf. The

171 latter is clearly depicted in the gravity field by 450x270 km rhomboid-shaped positive gravity
172 anomaly E (Fig. 1).

173 The Anisin Rift forms the northern part of the Anzhu Rift Zone. As illustrated by the MAGE
174 A4 Profile, it is an asymmetric feature with a single westerly dipping main detachment fault,
175 the IB Kapitan Dranitsin Fault of Franke et al. (2001), which is located along its eastern
176 flank, and a number of antithetic normal faults forming its western margin. It is clearly
177 depicted in the gravity field as a north to south striking c. 215-km-long negative anomaly
178 (Fig. 1). The southern part of the rift is confined to the 25 to 55-km-wide Zarya Half-graben,
179 while the northern part of the rift, north of 77°N, is represented by a much broader region of
180 extension that varies in width from 100 to 130 km. From north to south, the length of the rift,
181 including its inferred northern part, is c. 340 km. Sediment infill thickness varies from 2 km
182 along the western flank of the rift to up to 5 km along the MAGE A4 Profile and over 5 km in
183 its northern part.

184 **The Bel'kov-Svyatoi Nos (or just Bel'kov) Rift is separated** from the Anisin Rift by the
185 **Bel'kov Horst. It stretches for c. 430 to 450 km from an area northwest of Bel'kovsky Island,**
186 where it branches out from the Anisin Rift, to the Svyatoi Nos Cape on the southern shore of
187 the Dmitri Laptev Strait. A 175-km-long northern part of the rift has a maximum width of c.
188 75 km and consists of three parallel half-grabens, with the main west-faced detachment fault
189 located just off the west **coast of Bel'kovsky Island. This part of the rift is represented by one**
190 **of the most prominent gravity lows just west of Bel'kovsky Island, where the rift has the**
191 **thickest sediment fill of c. 5.5 km (Drachev et al. 1998; Franke et al. 2001).**

192 About 25 km **south of the southern tip of Bel'kovsky Island, the rift experiences a sharp** 45 to
193 50° bend towards the SE, and continues in this direction for 275 km between the Stolbovoi
194 **Horst in the west and the Kotel'nyi High in the east.**

195 New Siberian Rift

196 The New Siberian Rift is the easternmost element of the LRS. It stretches for c. 400 km in a
197 NW to **SE direction between the two most contrasting basement highs: the Kotel'nyi and De-**
198 Long Highs in the west and east, respectively (Fig. 1). The rift has a profoundly asymmetric
199 profile, with the main detachment fault located at its eastern flank separating the rift from the
200 De-Long High (Franke & Hinz 2009; Drachev, 2011). The rift's width is 120 to 130 km, and
201 the MAGE A4 Profile provides an almost complete cross-section of it, with the exception of
202 the north-eastern margin of the rift where the profile stops c.10 km west of the main border
203 fault.

204 The interior of the New Siberian Rift is complicated by a 200-km-long and c. 15 to 30-km-
205 wide horst block that separates the western part of the rift, the Neben Graben of Franke et al.
206 (2001) and Franke and Hinz (2009), from the main rift axis. The total thickness of the rift
207 sedimentary infill decreases from over 10 km in the deepest northern part to less than 1 km in
208 **the vicinity of Novaya Sibir' Island, where the rift terminates (Franke & Hinz 2009; Drachev**
209 2011).

210

211 The stratigraphy of the LRS is a highly speculative matter due to the complete lack of deep
212 wells offshore and the very fragmentary and incomplete Upper Cretaceous and Cenozoic
213 stratigraphic record preserved onshore. The most recent summary of the seismic stratigraphy
214 of the Laptev Shelf has been published by Drachev and Shkarubo (2017), and for the purpose
215 of this paper, we adopt stratigraphy from their publication. The sedimentary fill of the ULRB
216 is comprised of three major seismic units (Fig. 2): (i) a syn-rift Laptev Lower Unit (LLU) of
217 inferred Upper Cretaceous–lower Eocene age, which was deposited during both stretching
218 and thinning rift phases; (ii) a post-rift Laptev Middle Unit (LMU), which was deposited
219 during the rift stalled phase (this term was proposed by Van Wijk and Blackman, 2005) in the

220 latest Eocene–mid-Miocene (the age is based on our knowledge of the interaction between the
221 North American and Eurasian Plates; Savostin & Karasik 1981; Gaina et al. 2002; Glebovsky
222 et al. 2006); and (iii) a Laptev Upper Unit (LUU), which forms a continuous cover over the
223 entire Laptev Shelf and was accumulated during the second late Miocene–Pleistocene stage
224 of extension.

225 The timing of crustal extension onset is also unclear. As shown by Drachev (2002) and
226 Drachev and Shkarubo (2017), the pre-rift basement mainly formed during the late Mesozoic
227 (Late Jurassic–earliest Cretaceous) orogeny. Aptian and Albian continental coal-bearing
228 sediments known from **Kotel’nyi Island and Chukotka (Sokolov 2010; Kos’ko et al. 2013)**
229 are the oldest post-orogenic formations, which rest with a sharp angular unconformity upon
230 rocks that have been subjected to contractional deformation. These sediments do not provide
231 evidence in favour of their accumulation in a rift setting and, therefore, should be considered
232 as pre-rift deposits.

233 The oldest sediments documented in several small grabens in the coastal areas of the North
234 Verkhoyansk Mountains and the Yana-Indigirka Lowland are continental clastic sediments of
235 Paleocene age (Grinenko 1989). Therefore, the rift setting should have been initiated
236 sometime between the latest Early Cretaceous and the Paleocene, perhaps sometime in the
237 Late Cretaceous. An important recent finding of a Cenomanian-Turonian volcanic centre in
238 the North Verkhoyansk Mountains (Prokopiev 2013) may provide evidence in favour of the
239 rift onset occurring in the earliest Late Cretaceous.

240 **Seismic and Gravity Data Used for Modelling**

241 For the purpose of this study, we have used three multichannel seismic reflection profiles
242 oriented quasi-orthogonally to the shelf extensional fabric (Fig. 2). The MAGE A4 and TGS
243 ARS10F04 Profiles were acquired between 2008 and 2010 and cross almost the entire rift

244 system the central and NE parts of the Laptev Sea, with the exception of the western flank of
 245 the ULRB (Fig. 1)., The BGR 9701 Profile was acquired in 1997, and its interpreted depth-
 246 converted version was published by Franke et al. (2001).

247 For the gravity modelling, we have implemented time to depth conversion of the MAGE and
 248 TGS profiles. Velocities in the sedimentary cover were derived from seismic stacking
 249 velocities, which provide an adequate control for depths up to the length of the seismic
 250 streamers (c. 8 km). Below 8 km, we have used published seismic refraction data from the
 251 Laptev Sea (Franke et al. 2001) as well as refraction data from the North Chukchi Basin
 252 (Sakulina et al. 2011); the latter is filled with Cretaceous and Cenozoic siliciclastic sediments
 253 (Drachev 2016). The range of the velocities used is shown in Table 1.

254

255 **Table 1.** P-wave acoustic velocities used for time to depth conversion of MAGE A4 and TGS
 256 ARC10F04 seismic reflection profiles, along with the densities used in the gravity modelling

Layer\block	Interval seismic velocity used for Time/Depth conversion (km/s)	Density (g/cm ³)	Velocity calculated from density (km/s)
Sea water	1.5	1.03	1.5
Sedimentary unit LUU	1.8 to 5.5	2.10	2.52
Sedimentary unit LMU		2.30	3.39
Sedimentary unit LLU		2.56	5.16
Sedimentary unit LLU below c. 11 km in axial part of the ULRB (TGS ARS10F04 model only)	-	2.63	
Inferred weakly deformed Pz and Mz sedimentary rocks of outer Palaeo-Siberia passive margin	-	2.65	5.67
Inferred deformed Pz and Mz sedimentary rocks of outer Palaeo-Siberia passive margin and accreted terranes	5.6 to 6.25	2.74	6.10
Deformed Pz and Mz sedimentary rocks of proximal Palaeo-Siberia passive margin	-	2.76	6.19
'Non-Siberian' lower crust beneath late Mz fold belts	6.4 to 7.1	2.90	6.76
Lower crust of Palaeo-Siberian continent	-	3.00	7.11
Serpentinized upper mantle	6.9 to 7.5	3.10	7.43

Upper mantle	8.0	3.30	8.00
--------------	-----	------	------

257 The gravity data used for the 2D models was derived from a merge of the Getech reprocessed
 258 satellite altimeter gravity data set offshore and gridded gravity data onshore (Green &
 259 Fairhead 1996; Fairhead et al. 2004) as well as public-domain data from the Arctic Gravity
 260 Project (Kenyon et al. 2008). The data sets were merged into a single coherent 2 km grid that
 261 includes Bouguer anomaly and free-air anomaly data onshore and offshore, respectively. The
 262 Bouguer reduction density of the final grid (onshore part only) was 2.67 g/cc. It should be
 263 noted that although the gravity is presented as a 2 km grid, the resolution of the satellite
 264 gravity data set is c. 12 km minimum wavelength, with increasing noise at wavelengths below
 265 20 km.

266 Gravity Modelling

267 The 2D/2.5D gravity modelling permits testing of geological/seismic models against the
 268 observed gravity field. For this study, we used the Geosoft GM-SYS 2-D forward-modelling
 269 package with model layers of infinite length. This approach is justified because the main
 270 geological structures modelled (rifts) show no short-distance along-strike variability that may
 271 produce out-of-plane effects influencing the models. Since the modelled sections are located
 272 entirely offshore, we used the free-air gravity anomalies. The modelling technique enabled
 273 conversion of the interpreted seismic units/horizons into geological bodies within the model.
 274 Each of these bodies appeared as a polygon with an assigned density value. The software
 275 calculates the gravity response of the model using the technique outlined by Talwani and
 276 Ewing (1960). The gravity response from a proposed model was compared with the observed
 277 gravity; the model was then interactively adjusted until a satisfactory fit was obtained
 278 between the synthetic response and the observed gravity profile.

279 Gravity models are non-unique, which means that there are a multitude of density and
280 geometrical configurations that can produce the same amplitude and wavelength anomaly.
281 However, by using seismically constrained boundaries and geologically reasonable densities
282 for the modelled bodies down to the Moho, we are able to minimize the number of possible
283 outcomes. The range of rock densities (Table 1) is adopted from a previous modelling study
284 by Mazur et al. (2015) as well as being calculated from seismic interval velocities using a
285 Nafe-Drake formula (Ludwig et al. 1970; Brocher 2005).

286 The boundaries of the modelled bodies down to the top of pre-rift upper Mesozoic basement
287 inclusive are guided by seismic interpretation. These boundaries are considered to be reliable
288 along most of the modelled profiles, except for the deepest central zone of the ULRB.
289 Therefore, we tend to preserve these interpreted seismic boundaries while performing the
290 modelling.

291 The depth to the Moho is also fairly well constrained by the seismic data along significant
292 parts of the MCS profiles. However, where the Moho was not observed in the seismic record,
293 its depth was estimated by fitting the observed and calculated gravity data.

294 The least constrained seismic boundary is the Mid-Crust Discontinuity (MCD) due to
295 homogeneity of the seismic image of the basement over most of the interpreted seismic
296 profiles; however, some parts of the seismic profiles do have a higher reflectivity in the lower
297 section, which is interpreted as a possible indicative feature of the lower crust.

298 We also introduce some degree of first-order heterogeneity to crustal densities beneath both
299 the western flank and axial zone of the ULRB, and the crust to the east of the axial zone. This
300 is mainly based on an assumption that the western flank of the ULRB could be underlain by
301 the deformed margin of the ancient Siberian palaeocontinent with Lower Proterozoic high-
302 grade metamorphic complexes present at the lower crust level and deformed dense lower

303 Palaeozoic carbonate rocks present in the upper crust. Contrarily, the Eastern Laptev Shelf
304 basement could consist of less dense deformed Permian to Jurassic siliciclastic rocks that
305 were deposited along the distal part of the Palaeo-Siberian margin and in the troughs situated
306 between colliding terranes and the margin. The old Siberian metamorphic crust could be
307 completely absent in this tectonic domain.

308 There are a few localities where the seismic record demonstrates the presence of some weakly
309 deformed sedimentary successions directly beneath the top basement discontinuity (Franke et
310 al. 2001). We interpret these occurrences as moderately deformed pre-rift siliciclastic
311 sedimentary rocks of either Jurassic–Early Cretaceous or latest Early Cretaceous (Aptian to
312 Albian) age. The analogues of the former are exposed on Stolbovoi Island, while the latter are
313 known to be present in the central part of **Kotel’nyi Island (Kos’ko et al. 2013)**. We used
314 lower densities for these pre-rift sedimentary bodies (Table 1).

315 While performing the modelling, we tried to avoid introducing significant changes to the
316 seismically well-constrained horizons bounding seismic units LLU, LMU and LUU, and to
317 the Moho at points where it is detectable in the seismic record. Most modifications were
318 introduced to the MCD as it was the least constrained boundary. The consistency between the
319 seismic boundaries and the model was interactively achieved through a number of iterations
320 in the process of integrated interpretation.

321 **Results**

322 The resulting gravity models are presented in Figs. 3 to 5. The gravity synthetic response of
323 the models is low-pass filtered using a 20 km cut-off wavelength. This is done to remove the
324 gravity effect caused by the short-wavelength features of the seismic horizons used to build
325 the models. The resolution of the observed gravity (offshore gravity is mostly based on
326 satellite altimetry data) is insufficient to fully resolve <20 km wavelengths (see also Childers

327 et al. 2001). Furthermore, the short-wavelength signal is additionally smoothed out by the
328 gridding algorithm. Therefore, the observed gravity is mostly unable to replicate the short-
329 wavelength geometries revealed by seismic reflection horizons. However, in the range of the
330 long-wavelength anomalies (>20 km), which are mostly caused by the irregularities of the
331 Moho and the MCD as well as by large basement highs and depressions, there is a
332 satisfactory fit between the modelled and observed gravity along all the modelled profiles.

333 [TGS ARS10F04 Profile](#)

334 Model (a) along the TGS Profile (Fig. 3a) confirms the initial seismic interpretation by
335 allowing for the continental crust to be entirely thinned out in the axial part of the rift where
336 the sedimentary fill is directly underlain by upper continental mantle. Since the latter is no
337 longer protected by the crust from exposure to fluids circulating in the sedimentary fill, we
338 introduced a body of serpentized upper mantle with reduced density beneath the rift axis.
339 The Moho descends from c. 13 km in the centre of the ULRB to 27 km beneath the rift flanks.
340 An important misfit of c. 3 km **between the 'seismic' and the modelled Moho** is observed at
341 the eastern end of the profile. Additionally, the modelled base of the inferred serpentized
342 mantle below the ULRB is 4 km shallower than the inferred seismic boundary. This may
343 result from the poorly constrained velocity structure of the continental crust and mantle
344 underlying the LRS.

345 The MCD is located at depths of between 12 and 18 km. It shows no discernible trend of
346 depth variation beneath most of the ELHGP, being primarily located at depths of 15 to 16 km
347 except for two half-grabens bordering **the Bel'kov Horst**. Along the SW margin of the ULRB,
348 the MCD clearly deepens in SW direction.

349 In order to achieve a tighter fit between the observed and calculated gravity, we needed to
350 introduce a discrete sedimentary body with an increased density of 2.63 g/cm^3 at the base of
351 the ULRB depocentre underlain by the exhumed mantle. We assume that this body could

352 represent a sedimentary section intruded by mafic sills. Despite the fact that there is no
353 proven evidence of syn-rift magmatism known anywhere in the Laptev Sea region, one can
354 expect that it occurred within the hyperextended zone of the rift.

355 Model (b) demonstrates an alternative model that maintains a satisfactory fit between the
356 observed and calculated gravity without a body of serpentized mantle below the rift axis
357 (Fig. 3b). The main difference between the two models is the presence of the thicker lower
358 crust that underlies the central zone of the ULRB and counterbalances the absence of mantle
359 with reduced density that is included in model (a). To achieve a reasonable fit with the
360 calculated gravity, we needed to lower the base of sediments by 1 km and introduce a
361 significant amount of the lower crustal material below the seismically defined detachment.
362 The geometry of the latter is considerably steeper when it cuts through the lower crust as
363 compared to model (a).

364 [MAGE A4 Profile](#)

365 The modelled crustal section along the MAGE A4 Profile, which is located c. 60 to 100 km
366 south of the TGS Profile in the hyperextended zone of the ULRB, confirms the presence of a
367 12 to 15-km-thick sedimentary fill in the axial part of the basin that is underlain by the
368 severely stretched upper crust and exhumed lower crust (Fig. 4). In model (a), the Moho is
369 located at depth of c. 19 to 23 km under the hyperextended zone of the rift and at 25 to 30 km
370 under the ELHGP, and it is characterized by a fairly good fit between the seismically picked
371 and modelled Moho.

372 The modelled MCD below the ELHGP fluctuates at depths of between 12 and 18 km, with no
373 visible trend to the depth variation, and it demonstrates a **major misfit with the 'seismic'**
374 MCD due to the unconstrained nature of the latter. At the SW margin of the rift basin, the
375 MCD deepens in a SW direction from c. 15 km to 18 km at the end of the profile.

376 There are also some local misfits between the seismically observed and modelled top of the
377 basement horizon at the eastern flank of the rift, as well as the top of the exhumed lower
378 crustal block that has to be up to c. 2 km deeper than the inferred seismic horizon to allow for
379 a better fit.

380 The New Siberian Rift is filled with c. 11 km of syn-rift and post-rift sediments and it is
381 clearly associated with an asymmetric perturbation within the upper and lower crust. In this
382 area, the total thickness of the upper and lower crust is reduced to 11 km.

383 In model (b), we tested an alternative scenario that allows for a greater extent of the upper
384 crust layer below the ULRB (Fig. 4b). We assumed a different geometry for the main
385 detachment fault that remains an intracrustal detachment below the entire stretch of the
386 ULRB. To maintain a good fit between the calculated and the observed gravity, we needed to
387 significantly reduce the lower crust thickness by replacing it with the upper mantle to
388 counterbalance the effect of thicker upper crust above the detachment fault.

389 BGR 9701 Profile

390 The BGR 9701 Profile is located between the TGS ARS10F04 and MAGE A4 Profiles,
391 running parallel to the latter and traversing the entire axial zone and eastern flank of the
392 ULRB. The published interpretation of this profile (Franke et al. 2001) allows for much
393 thicker pre-rift continental crust to be present below the entire rift basin, which clearly
394 contradicts the modelled profiles located just to the south and north of the BGR 9701 Profile.
395 To resolve this contradiction, we tested three crustal models for the BGR 9701 Profile (Fig.
396 5).

397 In the BGR 9701 original interpretation (Fig. 5a), the ULRB appears as a broad feature with
398 two 25 to 35-km-wide grabens and a dividing basement horst in its central part. The sediment
399 thickness reaches c. 14 km in the grabens, reducing to 10 km over the central horst. The

400 Moho depth at the flanks of the basin is constrained by the seismic refraction data and varies
401 from 25 to 22 km, deepening away from the axial part of the ULRB; no Moho is detected
402 right beneath the central portion of the profile. The thickness of the continental crust beneath
403 the ULRB varies from c. 17 km at the SW end of the profile to 9 to 10 km below the axial
404 grabens, and to over 22 km at the NW end of the profile.

405 Model (a) demonstrates the calculated gravity response from the published interpretation of
406 the BGR 9701 Profile by Franke et al. (2001). As this interpretation postulates roughly flat
407 Moho and a quasi-uniform lower crust thickness, top basement geometry becomes the most
408 important factor controlling the gravity response along the model. Consequently, two major
409 lows of the forward-calculated gravity profile are located above the axial grabens. At the
410 same time, a significant synthetic gravity high is aligned with the NE portion of the profile,
411 where the thickest crust and the rise in Moho are inferred to be present. These three parts of
412 the model are the regions with the biggest misfits between the observed and calculated
413 gravity. At the same time, the observed gravity high above the axial grabens clearly implies
414 significant crustal thinning, which is in contrast to Franke et al.'s (2001) interpretation,
415 whereas the observed flat gravity profile above the M/V Lazarev Fault indicates that it has no
416 impact on the Moho configuration.

417 In order to produce a better fit between the observed and calculated gravity, we needed to
418 introduce significant modifications to the Franke et al. (2001) interpretation (Figs. 5b and c).
419 The crustal thickness is reduced west of the main detachment fault by deepening the top of
420 the basement horizon (LS1 horizon of Franke et al., 2001) and raising the Moho from c. 25 to
421 c. 16 km. In the original interpretation, the LS1 horizon was picked in the 3.5 to 6 km depth
422 range along the eastern flank of the ULRB, which is considerably shallower in comparison to
423 its depth in the TGS and MAGE profiles (5 to 11 km and 7.5 to 11 km, respectively). To
424 obtain a satisfactory fit between the modelled and observed gravity data, we had to infer a

425 deeper top basement boundary, which requires adding c. 1 to 4 km (in one location, it is up to
426 7 km) of syn-rift sediments.

427 The two resulting best-fit models (b) and (c) demonstrate significant crustal thinning below
428 the axial grabens: up to 5 to 6 km of the total crust thickness in model (b) and 2 to 4 km in
429 model (c), mainly accommodated by the rise in the Moho. The main difference between the
430 two models is the presence of upper crust below the axial grabens in (b), while upper crust is
431 completely removed in (c) and exhumed lower crust is inferred to underlie the deepest parts
432 of the grabens. Accordingly, the upper crust below the axial grabens in (b) is converted into
433 the lower part of sediments filling both grabens in (c). To achieve a better gravity fit in model
434 (c), additional Moho uplift is also introduced.

435 Additional changes introduced to the original 'seismic' model are related to the geometry of
436 the main detachment fault that is inferred to underlie, as a mid-crust detachment, the entire
437 ULRB eastern flank. It is further speculated that the detachment cuts through the lower
438 continental crust along the eastern flank of the crustal block) that may represent an H-block of
439 Lavier and Manatschal (2006) and Péron-Pinvidic and Manatschal (2010).

440 Discussion

441 The integration of the recently acquired long-offset seismic profiles with 2D gravity forward
442 modelling provides a much more reliable tool for deciphering the crustal architecture of the
443 LRS. While seismic data tightly constrain intrasediment horizons and, in most cases, the top
444 basement horizon, the gravity modelling provides valuable insights into the configuration of
445 the Moho, MCD and the top basement morphology. The combination of both methods allows
446 a successful portrayal of the full crustal section and overcomes the limitations of seismic
447 imaging.

448 The depth-converted seismic profiles accompanied by 2D gravity models reveal the presence
449 of hyperextended crust beneath the ULRB; its presence is characterised by Moho uplift and
450 thinning of the pre-rift crust. Moho uplift and crustal thinning were compensated by vast
451 subsidence of the rift basins, creating accommodation space for as much as 12 to 14 km of
452 syn- to post-rift sediments.

453 The results obtained illustrate a brittle mode of upper crustal stretching that is demonstrated
454 by the presence of tilted basement blocks bounded by listric normal faults on both sides of the
455 rift axis. In contrast, the lower crust experienced ductile thinning, which is suggested by a
456 gradual reduction in crustal thickness towards the rift axis. In the southerly located MAGE
457 A4 and BGR 9701 Profiles, the upper crust may be entirely thinned out and the lower crust is
458 exhumed at the base of sedimentary section. Along the northernmost TGS ARS10F04 profile,
459 the modelling revealed even more advanced crustal stretching that led to the exhumation of
460 the upper continental mantle beneath the rift sedimentary fill, which was predicted by the
461 earlier gravity modelling (Mazur et al. 2015).

462 In a magma-poor rift setting reviewed by Franke (2013), lithospheric extension in response to
463 divergent plate movements did not result in a significant heat input from the asthenospheric
464 mantle. The LRS is a typical magma-poor rift zone, and our results suggest that there was
465 almost complete break-up of the crust prior to the break-up of continental mantle. This
466 situation seems to reflect an initiation of mantle exhumation, which is a feature that is widely
467 documented for mature magma-poor continental margins (e.g. Whitmarsh et al. 2001;
468 Manatschal et al. 2010). Consequently, the LRS corresponds to an embryonic non-volcanic
469 margin, where pre-rift crust has been mostly or entirely eliminated across the rift axis but
470 continental mantle has not yet broken up.

471 Using the modelled cross-sections, which provide much more reliable constraints over the
472 crustal architecture of the LRS than any of the previously published seismic interpretations,
473 we were able to estimate the amount of total net crustal extension for all the models. The
474 amount of stretching was calculated based on the method outlined by Mazur et al. (2012), i.e.
475 through reconstructing the crust to its pre-rift thickness, which is assumed to be 35 km. This
476 calculation estimated the finite crustal extension to be 315 km along the MAGE A4 Profile,
477 320 km along the TGS ARS10F04 Profile, and 235 km along the BGR 9701 Profile. Due to
478 the fact that none of the modelled profiles cross the entire width of the LRS, the obtained
479 values can only be considered as minimum extension values along the modelled profiles and
480 they do not represent total extension values across the entire rift system; nevertheless, they
481 provide a good match with the extension estimate based on 3D gravity inversion (Mazur et
482 al., 2015; pseudo-section 3 in their table 1).

483 Conclusion

484 The LRS remains one of the least studied present-day geodynamic settings where a divergent
485 plate boundary crosses a continental margin and causes a transition from ocean floor
486 spreading to intracontinental rifting. Therefore, the Laptev Sea provides a unique opportunity
487 for studying all stages of continental break-up, from initial stretching to mantle exhumation
488 and the initiation of seafloor spreading.

489 Recent advances in seismic data acquisition in the Russian Arctic led to much better imaging
490 of the sedimentary fill and consolidated basement of the LRS. However, the existence of sub-
491 marine permafrost and intense faulting limit seismic data resolution at depths greater than 8 to
492 10 km. This, in turn, makes any models of the LRS tectonics that are based entirely on
493 seismic data very unreliable.

494 Our study presents the first results of seismic and gravity data integration. **The study's aim**
495 was to provide reliable constraints on the crustal architecture of this rift system. The
496 modelling performed allowed us to test the hypothesis of mantle exhumation proposed by
497 Mazur et al. (2015) and Drachev and Shkarubo (2017). According to our results, there is little
498 chance that pre-rift continental crust is preserved in the NW part of the ULRB north of 75°N
499 and west of 130°E. Although a very thin layer of the lower continental crust is still
500 reconcilable with the gravity response along the TGS ARS10F04Profile (Fig. 3b), this
501 scenario is highly unlikely since it would require the lower crust to have very low viscosity.

502 The relatively low resolution of the satellite altimeter-derived gravity data used in this study,
503 the poor resolution of the seismic data in the deepest part of the ULRB, and the scarcity of
504 wide-angle deep seismic refraction data mean that the crustal models presented here can only
505 be considered as a first rough representation of the crustal architecture of the LRS. Should the
506 modern long-offset seismic reflection and refraction experiments be carried out in the future,
507 along with the acquisition of ship-born gravity data, much tighter constrained models could
508 be produced. However, the importance of the results presented in this paper is in
509 demonstrating that some previously published models, postulating the presence of thinned but
510 still continuous continental crust throughout the entire rift system, are not sufficiently
511 accurate.

512 **Acknowledgements**

513 The authors are thankful to MAGE and TGS for granting permission to use their seismic
514 profiles in this publication. Getech is thanked for providing the gravity data.

515 We also thank A. Scot and the anonymous reviewer for providing us with a number of
516 important critical comments that let us improve the manuscript. Our special thanks are to
517 Katie Spike (Getech) who performed a scrupulous editing of the manuscript.

518 Referenc es

- 519 Brocher, T.
M. 2005. Empirical Relations between Elastic Wavespeeds and Density in the
- 520 **Earth's Crust**. Bulletin of the Seismological Society of America, 95, 6, 2081-2092, doi:
521 10.1785/0120050077.
- 522 Brun, J. P. & Beslier, M. O. 1996. Mantle exhumation at passive margins. Earth and
523 Planetary Science Letters, 142, 1, 161-173.
- 524 Childers, V. A., Mcadoo, D. C., Brozena, J. M. & Laxon, S. W. 2001. New gravity data in the
525 Arctic Ocean: Comparison of airborne and ERS gravity. Journal of Geophysical
526 Research, 106, 8871-8886.
- 527 Drachev, S. S. 2002. On the basement tectonics of the Laptev Sea Shelf. Geotectonics, 36, 6,
528 483-498.
- 529 Drachev, S.S. 2011. Tectonic setting, structure and petroleum geology of the Siberian Arctic
530 offshore sedimentary basins. In: Spencer, A. M., Embry, A. F., Gautier, D. L.,
531 Stoupakova, A. V. & Sørensen, K. (eds.) Arctic Petroleum Geology. Geological Society
532 (London) Memoirs, 35, 369-394.
- 533 Drachev, S.S. 2016. Fold belts and sedimentary basins of the Eurasian Arctic. Arktos, online
534 publication, 30 pp.
- 535 Drachev, S. S. & Savostin, L. A. 1994. Structure and plate tectonics of the Laptev Sea Shelf:
536 drilling of the geological record. In: H. Kassens, H. W. Hubberten, S. Pryamikov and R.
537 Stein (eds) Reports on Polar Research. 144. Alfred Wegener Institute for Polar and
538 Marine Research, Bremerhaven, Germany, pp. 115-117.
- 539 Drachev, S. S., Savostin, L. A., Groshev, V. G. & Bruni, I. E. 1998. Structure and Geology of
540 the Continental Shelf of the Laptev Sea, Eastern Russian Arctic. Tectonophysics, 298,
541 357-393.
- 542 Drachev, S. S. & Shkarubo, S. I. 2017. Tectonics of the Laptev Shelf, Siberian Arctic. In:

543 Pease, V. & Coakley, B. (eds) Circum-Arctic Lithosphere Evolution. Geological
544 Society, London, Special Publications, 460, <https://doi.org/10.1144/SP460.15>.

545 Fairhead, J. D., Green, C. M. & Fletcher, K. M. U. 2004. Hydrocarbon screening of the deep
546 continental margins using non-seismic methods. *First Break*, 22, 11, 59-63.

547 Franke, D. 2013. Rifting, lithosphere breakup and volcanism: Comparison of magma-poor
548 and volcanic rifted margins. *Marine and Petroleum Geology*, 43, 63-87.

549 Franke, D. & Hinz, K. 2009. Geology of the shelves surrounding the New Siberian Islands,
550 Russian Arctic. *Stephan Mueller Spec. Publ. Ser.*, 4, 4, 35-44.

551 **Franke, D., Hinz, K., Block, M., Drachev, S. S., Neben, S., Kos'ko, M. K., Reichert, C. &**
552 **Roeser, H. A.** 2000. Tectonics of the Laptev Sea Region in North-Eastern Siberia. In:
553 Roland, N. W. & Tessensohn, F. (eds) III International Conference on Arctic Margins.
554 *Polarforschung*, 68, 51-58.

555 Franke, D., Hinz, K. & Oncken, O. 2001. The Laptev Sea Rift. *Marine and Petroleum*
556 *Geology*, 18, 10, 1083-1127.

557 Gaina, C., Roest, W.R. & Müller, R.D. 2002. Late Cretaceous-Cenozoic deformation of
558 northeast Asia. *Earth and Planetary Science Letters*, 197, 273-286.

559 **Glebovsky, V. Yu., Kaminsky, V. D., Minakov, A. N., Merkur'ev, S. A., Childers, V. A. &**
560 **Brozena, J. M.** 2006. Formation of the Eurasia Basin in the Arctic Ocean as Inferred
561 from Geohistorical Analysis of the Anomalous Magnetic Field. *Geotectonics*, 40, 4,
562 263-281.

563 Grachev, A. F. 1982. Geodynamics of the Transitional Zone from the Moma Rift to the
564 Gakkel Ridge. In: J. S. Watkins and C. L. Drake (eds) *Studies in Continental Margin*
565 *Geology*. *Am. Assoc. Pet. Geol. Mem.*, 34, 103-113.

566 Green, C. M. & Fairhead, J. D. **1996. New 5'×5' digital gravity and terrain models of the**
567 **Earth**, in *Global Gravity Field and its Temporal Variations*. In: Rapp, R. H., Casenave,

- 568 A. A. & Nerem, R. S. (eds) IAG Symposia, 116, Springer
- 569 Grinenko, O. V. (ed.) 1989. Palaeogene and Neogene of North-East of the USSR. Scientific
570 Center of Siberian Department of Academy of Sciences of USSR, Yakutsk (in Russian).
- 571 Ivanova, N. M., Sekretov, S. B. & Shkarubo, S. I. 1990. Geological structure of the Laptev
572 Sea shelf according to seismic studies. *Oceanology*, 29, 600-604.
- 573 Karasik, A. M. 1968. Magnetic anomalies of the Gakkel Ridge and the origin of the Eurasian
574 Subbasin of the Arctic Ocean. *Geophysical Survey Methods in the Arctic*. NIIGA,
575 Leningrad, 5, 8-19 (in Russian).
- 576 Karasik, A. M. 1974. The Eurasia Basin of the Arctic Ocean from the point of view of plate
577 tectonic. In: *Problems in geology of polar areas of the Earth*. Leningrad, Nauchno-
578 **Issledovatel'skii Institut Geologii Arktiki**, 23-31 (in Russian).
- 579 Kenyon, S., Forsberg, R. & Coakley, B. 2008. New gravity field for the Arctic. *Eos*
580 *Transactions American Geophysical Union*, 89, 32-, 289-290, doi:
581 10.1029/2008EO320002.
- 582 Kholodov, A. L., Romanovskii, N. N., Gavrilov, A. V., Tipenko, G. S. Drachev, S. S.,
583 Hubberten, H. W. & Kassens, H. **2001. Modelling of the offshore permafrost
584 thickness**
585 **Kos'ko, M. K., Sobolev, N. N., Korago, E. A., Proskurnin, V. F. & Stolbov, N. M. 2013.**
586 **Geology of New Siberian Islands – a basis for interpretation of geophysical data on the**
587 **Eastern Arctic shelf of Russia. *Neftegazovaya geologiya. Teoriya i praktika*, 8, 2, 1-36**
588 **(in Russian).**
- 589 Lavier, L. L. & Manatschal, G. 2006. A mechanism to thin the continental lithosphere at
590 magma-poor margins. *Nature*, 440, 324-328.
- 591 Ludwig, W. J., Nafe, J. E. & Drake, C. L. 1970. Seismic refraction. In: Maxwell, A. E. (ed.)

593 Manatschal, G., Sutra, E. & Péron-Pinvidic, G. 2010. The lesson from the Iberia-
594 Newfoundland rifted margins: how applicable is it to other rifted margins? Proceedings
595 of the II Central & North Atlantic Conjugate Margins Conference, Lisbon. Volume II,
596 27-37 (<http://metododirecto.pt/CM2010/>).

597 Mazur, S., Green, C., Stewart, M. G., Whittaker, J. M., Williams, S. & Bouatmani, R. 2012.
598 Displacement along the Red River Fault constrained by extension estimates and plate
599 reconstructions. *Tectonics*, 31, TC5008, doi: 10.1029/2012TC003174.

600 Mazur, S., Campbell, S., Green, C. & Bouatmani, R. 2015. Extension across the Laptev Sea
601 continental rifts constrained by gravity modeling. *Tectonics*, 34, 435-448. doi:
602 10.1002/2014TC003590.

603 Peron-Pinvidic, G. & Manatschal, G. 2010. From microcontinents to extensional allochthons:
604 witnesses of how continents break apart? *Petroleum Geoscience*, 16, 189-197.

605 Prokopiev, A. 2013. Structure and Late Mesozoic - Early Cenozoic Evolution of the
606 Verkhoysk and Olenek fold belts (Laptev Sea shore) Junction Z. AAPG Search and
607 Discovery Article #90177. ©3P Arctic, Polar Petroleum Potential Conference &
608 Exhibition, Stavanger, Norway, October 15-18, 2013.

609 Sakoulina, T. S., Verba, M. L., Kabushina T. B., Krupnova, N. A., Tabyrtsa, S. N., Ivanov, G.
610 I. 2011. Integrated geological-geophysical investigations along a reference line 5-AR in
611 the East Siberian Sea. *Razvedka i okhrana nedr*, 10, 17-23 (in Russian).

612 Savostin, L. A. & Karasik, A. M. 1981. Recent plate tectonics of the Arctic basin and of
613 northeastern Asia. *Tectonophysics*, 74, 111-145.

614 Sekretov, S. B. 2000. Petroleum potential of the Laptev Sea basins: Geological, tectonic and
615 geodynamic factors. In: N. W. Roland & F. Tessensohn (eds) III International
616 Conference on Arctic Margins. *Polarforschung*, 68, 179-186.

617 Shkarubo, S. I. & Zavarzina, G. A. 2011. Stratigraphic characteristics of seismic sequences in

618 the sedimentary cover of the western Laptev Sea shelf. *Neftegazovaya geologiya.*
619 *Teoriya i praktika*, 6, 2, 1-21 (in Russian).

620 Shkarubo, S. I., Zavarzina, G. A. & Zuikova, O. N. 2014. Results of modern stage of the
621 Laptev Sea shelf study: From hypotheses to new facts and challenges. *Okhrana i*
622 *Razvedka Nedr*, 4, 23-30 (in Russian).

623 Sokolov, S. D. 2010. Tectonics of Northeast Asia: An Overview. *Geotectonics*, 44, 493-509.

624 Talwani, M. & Ewing, M. 1960. Rapid computation of gravitational attraction of three-
625 dimensional bodies of arbitrary shape. *Geophysics*, 25, 203-225.

626 Van Wijk, J. W. & Blackman, D. K. 2005. Dynamics of continental rift propagation: the end-
627 member modes. *Earth and Planetary Science Letters*, 229, 247-258.

628 Whitmarsh, R.B., Manatschal, G. & Minshull, T.A. (2001) - Evolution of magma-poor
629 continental margins from rifting to seafloor spreading. *Nature*, 413, 150-154.

630 Zavarzina, G. A., Shkarubo, S. I. Shlykova, V. V. & Poshtatskaya, A. G. 2014. New data on
631 tectonics of the Pritaimyr Shelf, Laptev Sea. *Okhrana i Razvedka Nedr*, 4, 31-34 (in
632 Russian).

633 Figure Captions

634 **Fig. 1.** The gravity field and the main structural elements of the Laptev Rift System. The

635 satellite altimeter gravity field (coloured background), which is comprised of free-air

636 anomaly offshore and Bouguer anomaly onshore, was compiled by Getech (Mazur et al.

637 2015 and references therein). The insert map in the left-hand-side lower corner shows

638 the plate tectonic setting of the studied area (black rectangle), the axis of the Gakkel

639 Spreading Ridge (bold red line), the axis of linear magnetic anomalies (after Glebovsky

640 et al. 2006) and earthquake epicenters (black circles) from

641 <https://earthquake.usgs.gov/earthquakes/search>. The Roman numerals denote the

642 following structural elements: I – Ust' Lena Rift: Ia – inferred zone of mantle

643 exhumation, Ib – Omoloy Graben; II – East Laptev Horst and Graben Province: IIa –

644 North Laptev High, IIb – Stolbovoi Horst, IIc – Shiroston High, IId – Ust' Yana Graben,

645 IIe – Central Laptev Terraces; III – Anzhu Rift Zone: IIIa – Anisin Rift, IIIb – Zarya

646 Graben, IIIc – Bel'kov-Svyatoi Nos Rift, IIId – Bel'kov Horst, IIIe – Kigilyakh Horst,

647 IIIf – Tas-Takh Graben; IV – New Siberian Rift: IVa – Neben Graben, IVb – Sannikov

648 Horst; V – Eurasia Basin rifted margin; VI – Eurasia Oceanic Basin: VIa – Amundsen

649 Basin, VIb – Nansen Basin; VII – Kotel'nyi Basement High; VIII – De Long Basement

650 High. The red Arabic numerals on the insert map denote the following geographic

651 features: 1 – Anabar Bay; 2 – Nansen Basin; 3 – Amundsen Basin; 4 – Buor-Khaya

652 Bay; 5 – Yana-Indigirka Lowland; 6 – **Kotel'nyi Island**; 7 – Stolbovoi Island; 8 –

653 **Bel'kovsky Island**; 9 – Svyatoi Noc Cape; 10 – Dmitri Laptev Strait; 11 – De Long

654 Islands; 12 – Novaya **Sibir' Island**; 13 – North Verkhoyansk Mountains.

655 **Fig. 2.** Geological cross-sections along the interpreted depth-converted seismic profiles used

656 for the gravity modelling. Cross-sections (a) and (c) are based on Drachev and Shkarubo

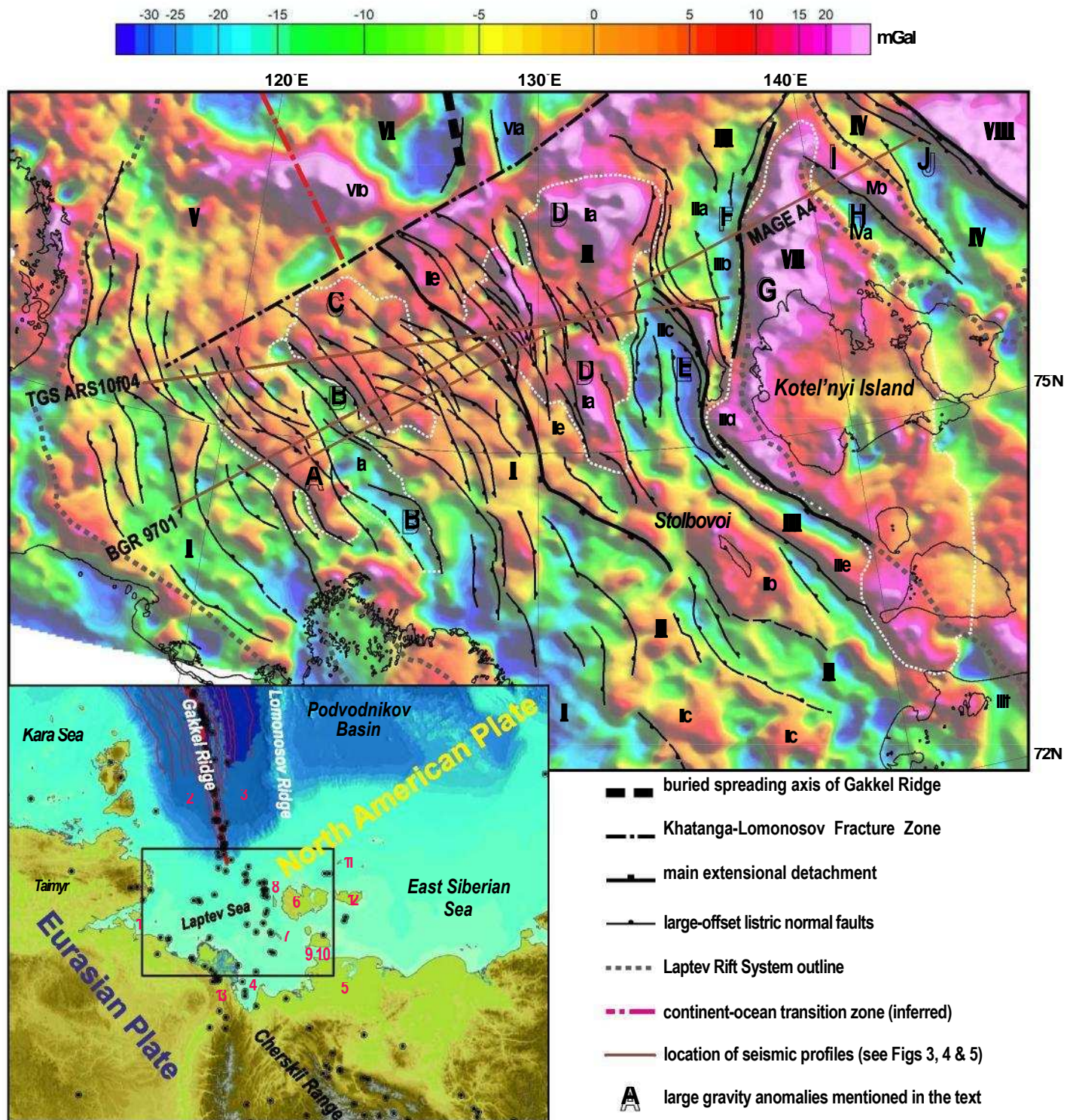
657 (2017); cross-section (b) is modified from Franke et al. (2001). See Fig. 1 for the

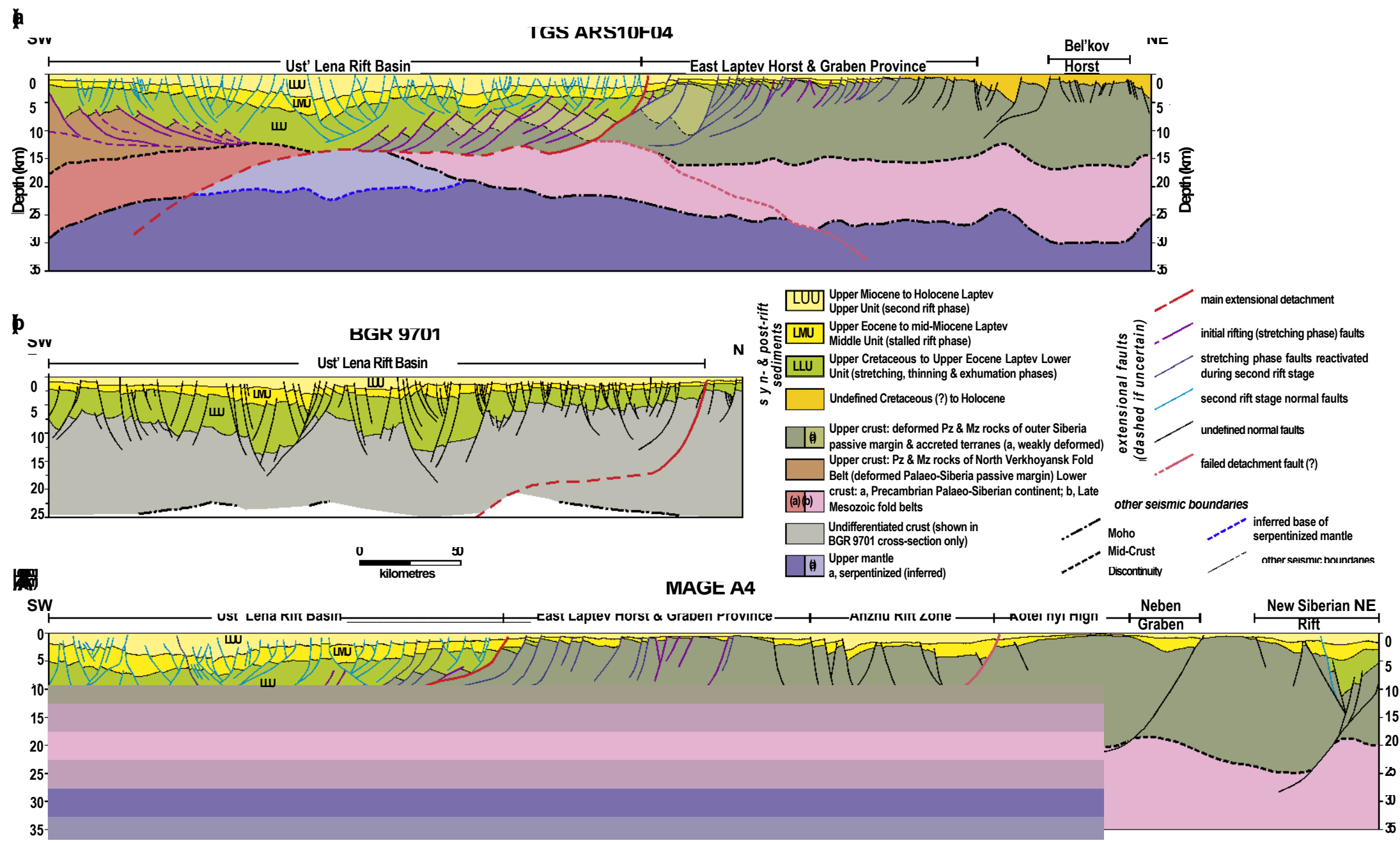
658 locations of the seismic profiles.

659 **Fig. 3.** Modelled crustal cross-sections along MCS Profile TGS ARS10F04 (see Fig. 1 for the
660 location). A legend explaining the colour of the polygons is given in Fig. 2. Model (a) is
661 based on the interpretation by Drachev and Shkarubo (2017; Fig. 2a), which assumes
662 that exhumed serpentinitized upper mantle is present underneath the sedimentary fill of
663 the ULRB. Model (b) tests an alternative scenario where thin lower crust is present at
664 the base of the ULRB. The dot-dashed magenta line corresponds to the Moho modelled
665 in model (a), i.e. showing the divergence between two models. Other modelled
666 boundaries fully coincide with model (a).

667 **Fig. 4.** Modelled crustal cross-sections along MCS Profile MAGE A4 (see Fig. 1 for the
668 location). A legend explaining the colours of the polygons is given in Fig. 2. Model (a)
669 tests the interpreted seismic profile given in Fig. 2c. Model (b) tests an alternative
670 scenario with upper crust present beneath the axis of the ULRB. The main detachment
671 fault is a low-angle fault that separates the lower and upper crust. Dashed and dot-
672 dashed magenta lines correspond to model the Mid-Crust Discontinuity and the Moho,
673 respectively (showing the divergence between the two models). Other modelled
674 boundaries fully coincide with model (a). For the complete legend, see Fig. 3.

675 **Fig. 5.** Modelled crustal cross-sections along MCS Profile BGR 9701 (see Fig. 1 for the
676 location and Fig. 3 for the complete legend). Model (a) is based on the interpretation by
677 Franke et al. (2001). It demonstrates a significant misfit between the calculated and
678 observed gravity. Models (b) and (c) are alternative models that provide a much tighter
679 fit between the observed and calculated gravity. Note that the modelled boundaries in
680 model (c) are shown only in places where they diverge from those modelled in (b); in all
681 other cases, they are equal to the seismic horizons and boundaries shown in model (b).





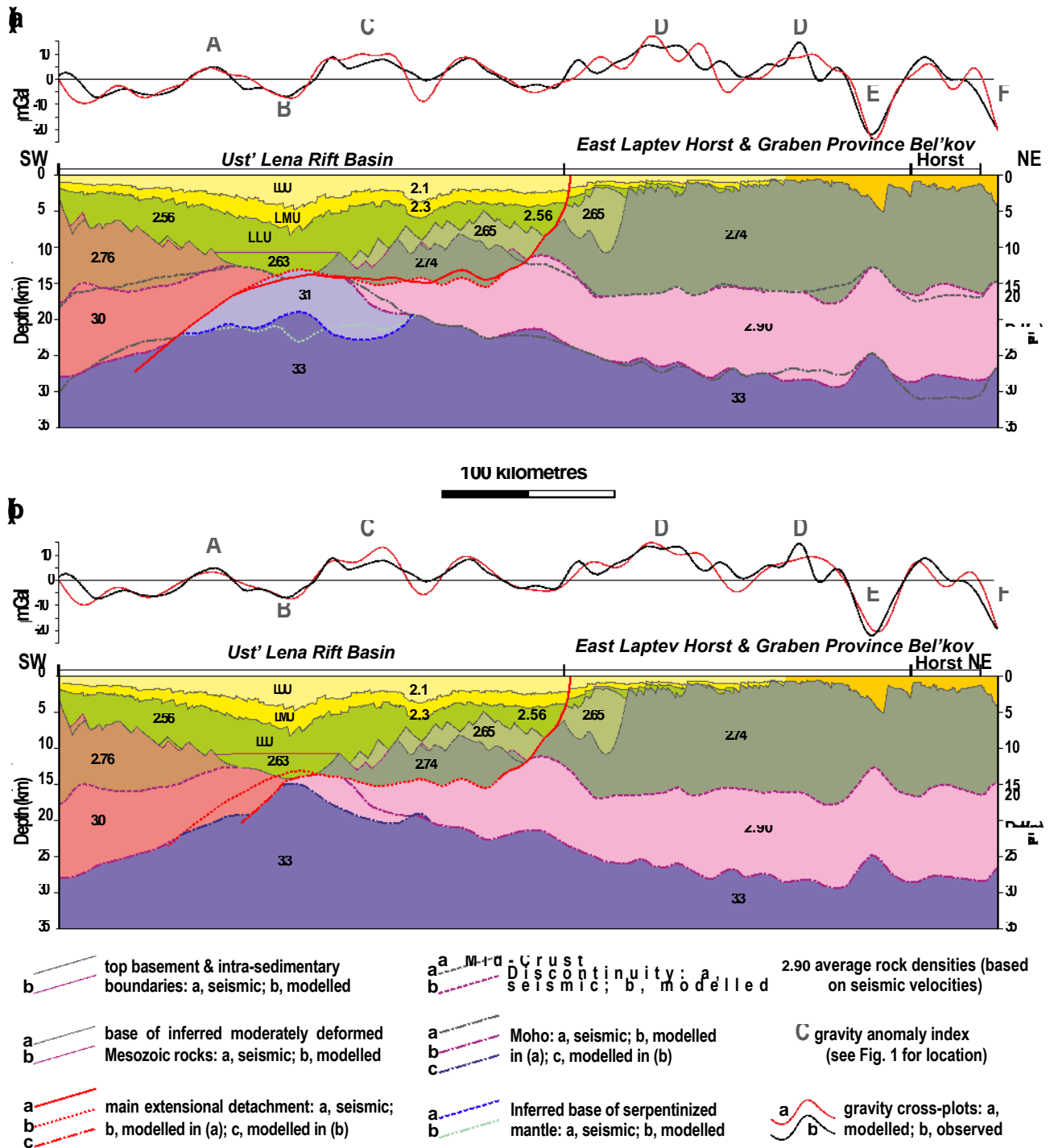
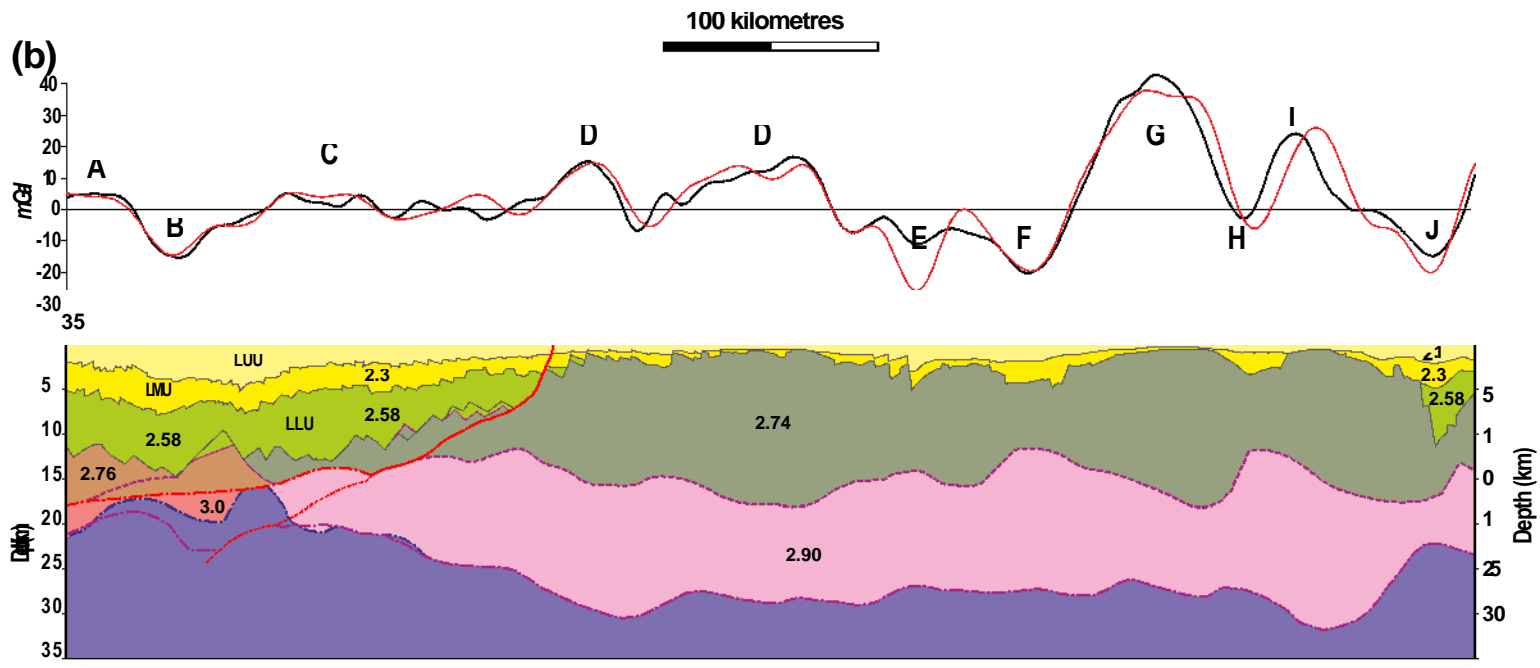
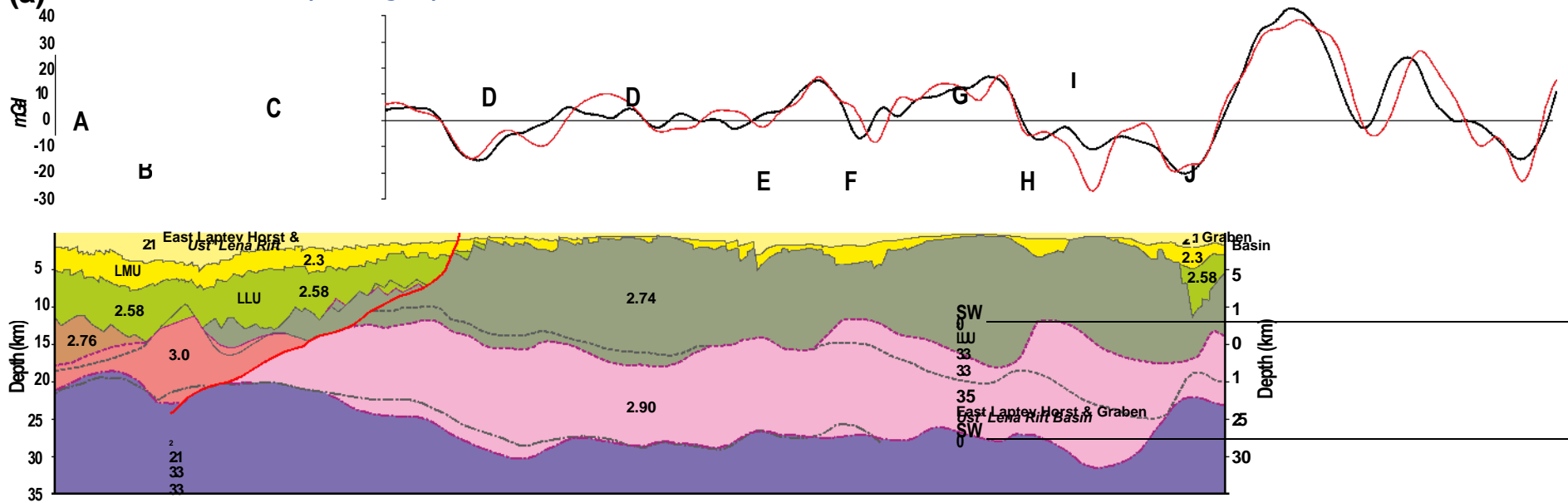


Figure 4

(a) [143_Drachev_etal_Laptev_FIG_4.pdf](#)



trace of main extensional detachment inferred by seismic data (shown in (b) for reference only)

